

Ultrasound-assisted synthesis of porous Co_3O_4 microrods and their lithium-storage properties

Dong Xie · Xiumei Du · Qingmei Su ·
Weiwei Yuan · Zimin Dong · Jun Zhang ·
Gaohui Du

Received: 22 May 2014 / Accepted: 11 December 2014
© Springer-Verlag Berlin Heidelberg 2014

Abstract Porous Co_3O_4 microrods have been prepared by an ultrasound-assisted route with subsequent calcination. The as-prepared Co_3O_4 microrods are composed of interconnected nanoparticles with porous characteristics. The ultrasonic irradiation is critical to determine the morphology and the electrochemical performance of the products. When tested as anode material for lithium-ion battery, the porous Co_3O_4 microrods show improved capacity and rate cycling performance. The reversible capacity of the materials retains $678 (\pm 5) \text{ mAh g}^{-1}$ after 50 cycles at 100 mA g^{-1} . Even when cycled at various rate for more than 50 cycles, the reversible capacity recovers to $600 (\pm 5) \text{ mAh g}^{-1}$ for the current of 100 mA g^{-1} . The improved lithium-storage performance can be attributed to the reduced electrochemical reaction resistance due to the unique porous architecture of Co_3O_4 microrods.

1 Introduction

Lithium-ion batteries (LIBs) have an increasingly diverse range of application from cars to microchips and are currently the dominant power sources for portable electronic devices. To meet the various application requirements, LIBs are required to have superior energy density, power density, and good cyclability. The growing demand

has stimulated intensive exploration of new electrode materials [1–3]. In particular, in situ technology has been developed to observe directly the electrochemical behavior of the electrode materials in order to reveal their reaction mechanism [3, 4]. Transition metal oxides are promising anode materials for LIBs owing to their high theoretical capacities and volumetric energy densities [5–7]. However, their applications have been hampered by the poor capacity retention upon cycling due to large volume expansion and severe particle aggregation during the Li^+ insertion and extraction process [3, 8]. One of the promising strategies to alleviate this problem is to fabricate nanomaterials with porous structures, which have high electrode–electrolyte contact area, short path length for Li^+ transport, and good strain accommodation as compared to solid nanostructures.

Co_3O_4 has received considerable attention as an anode material with high theoretical capacity (890 mAh g^{-1}). Great efforts have been made to fabricate novel Co_3O_4 porous nanostructures to improve the electrochemical properties. For example, various Co_3O_4 porous nanostructures, including polyhedral architectures [9], nanowires [10], platelets [11], flowers [12], hollow thin films [13], and urchin-like hollow spheres [14], have been reported and indeed exhibited enhanced electrochemical activity. So far, several methods have been developed to tailor the structures and thereby the electrochemical properties, including electrospinning [15], template [16], and hydrothermal methods [9]. In this article, we report a new ultrasound-assisted method to prepare uniform porous Co_3O_4 microrods with the advantages of high efficiency and low cost. Owing to the hierarchical architecture, the as-prepared Co_3O_4 exhibits improved reversible capacity, better rate, and cycling performance as an anode material in LIBs.

D. Xie · X. Du · Q. Su · W. Yuan · Z. Dong · J. Zhang ·
G. Du (✉)
Institute of Physical Chemistry, Zhejiang Normal University,
Jinhua 321004, China
e-mail: gaohuidu@zjnu.edu.cn

2 Experiments

2.1 Synthesis

All the reagents were of analytical purity and were used without further purification. $\text{Co}(\text{NO}_3)_2 \cdot 6\text{H}_2\text{O}$ and $(\text{NH}_4)_2\text{C}_2\text{O}_4 \cdot \text{H}_2\text{O}$ were purchased from Shanghai Zhanyun Chemical Ltd Co of China. In a typical synthesis, 50 mL of $\text{Co}(\text{NO}_3)_2 \cdot 6\text{H}_2\text{O}$ solution (0.2 M) was prepared in a beaker; then, 100 mL of $(\text{NH}_4)_2\text{C}_2\text{O}_4$ (0.1 M) solution was added into the beaker slowly under ultrasound irradiation (45 kHz and 100 W) at room temperature. Pink precipitation appeared after about 1 min, and the ultrasound irradiation continued for additional 30 min. Subsequently, the pink precipitate was centrifuged, washed with distilled water and absolute ethanol, and dried at 60 °C for 6 h. The formed precursors were put into a quartz boat and roasted at 500 °C for 1 h in a furnace to obtain the final products (denoted as S1). To investigate the influence of ultrasonic irradiation on the product and the electrochemical properties, a similar experiment was carried out without ultrasonic irradiation. The obtained product is denoted as S2.

2.2 Characterization

The products were characterized using X-ray powder diffraction (XRD) on a Philips PW3040/60 X-ray diffractometer with $\text{Cu K}\alpha$ ($\lambda = 1.5418 \text{ \AA}$) radiation for phase identification. The morphologies were examined using scanning electron microscopy (SEM) on a Hitachi S4800 microscope, and the microstructures were investigated using transmission electron microscopy (TEM) and high-resolution TEM (HRTEM) performed on a JEOL 2100F instrument at an acceleration voltage of 200 kV. The sample for TEM analysis was prepared by dispersing the final sample in ethanol; the suspension was then dropped on a copper grid covered with an amorphous carbon film.

2.3 Electrochemical measurement

The electrodes were prepared by dispersing the prepared products (S1 or S2) (75 wt%), acetylene carbon black (15 wt%), and poly(vinylidene fluoride) binder (10 wt%) in *N*-methyl-2-pyrrolidone solvent to form a slurry. The slurry was pasted onto Ni foam current collectors and dried at 80 °C for 6 h in a vacuum oven. The electrochemical measurements were carried out by two-electrode coin cells with lithium foil as the counter electrode. The CR2025-type coin cells were assembled in an argon-filled glove box. The electrolyte solution was 1 M LiPF_6 dissolved in a mixture of ethylene carbonate and dimethyl carbonate with a volume ratio of 1:1. Cyclic voltammetry (CV) and AC impedance measurements were carried out on a CHI 660C

electrochemistry workstation. The galvanostatic charge and discharge measurements were conducted on LAND battery test system at different current densities in the voltage range from 0.02 to 3 V. In addition, the capacity is calculated according to the mass of Co_3O_4 .

3 Results and discussion

The XRD patterns of the as-prepared precursors with ultrasonic irradiation and the two products are shown in Fig. 1. The refraction peaks of the precursors can be well indexed to $\text{CoC}_2\text{O}_4 \cdot 2\text{H}_2\text{O}$ (JCPDS No. 48-1068). As for the calcined product S1 and S2, the refraction peaks can be assigned to (111), (220), (311), (222), (400), (422), (511), (440) planes of the cubic Co_3O_4 (JCPDS No. 43-1003) with a space group of $Fd\bar{3}m$. No trace of other impurity was detected, indicating that the $\text{CoC}_2\text{O}_4 \cdot 2\text{H}_2\text{O}$ precursors converted to crystalline Co_3O_4 completely after calcination.

Figure 2a, b shows the SEM images of CoC_2O_4 precursors of sample S1, which consist entirely of microrods with diameters around 0.5–0.8 μm . The surfaces of CoC_2O_4 precursors are basically smooth without porous characteristics (Fig. 2b). The annealing treatment at 500 °C converted the precursor microrods to porous Co_3O_4 without any solid by-products as shown in Fig. 2c, d. It can be seen that the as-obtained Co_3O_4 maintains the microrod morphology. In contrast to the precursors, the surfaces of the Co_3O_4 microrods become rough and display a loose structure consisting of interconnected nanoparticles and inter-particle pores, which result from the decomposition of CoC_2O_4 precursor. Shown in Fig. 2e is a TEM image of Co_3O_4 microrods, further revealing that they are composed

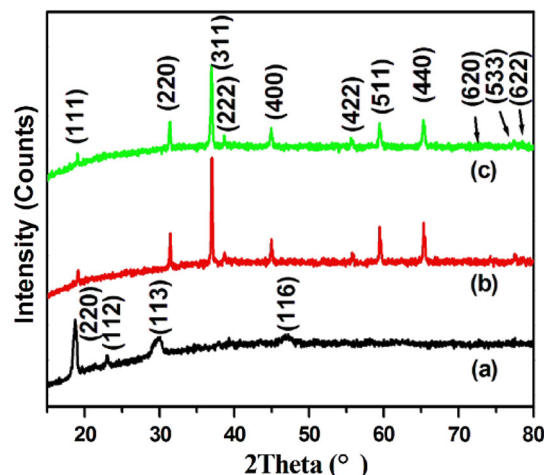


Fig. 1 XRD patterns of the precursors (a), the products S1 (b), and S2 (c)

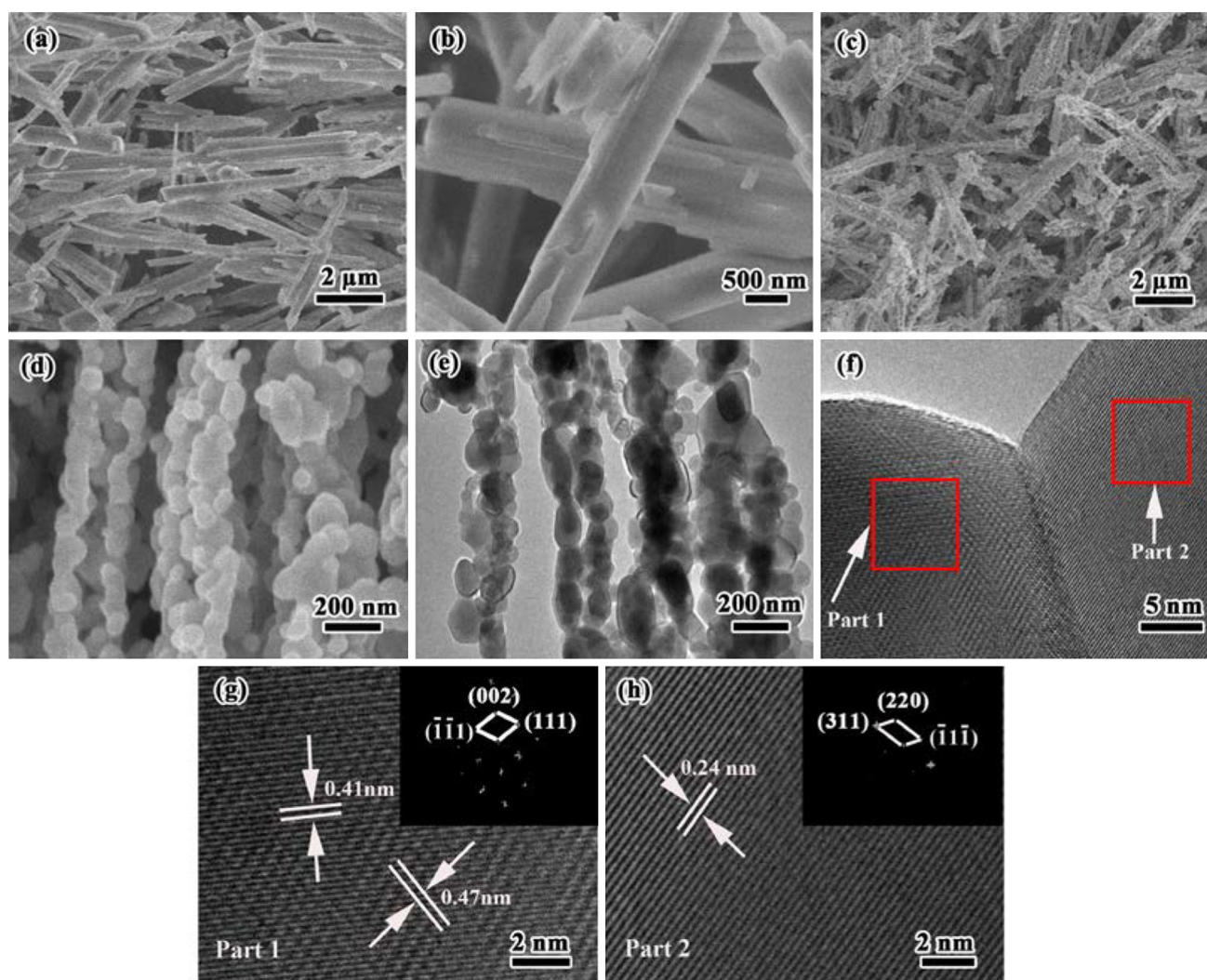


Fig. 2 SEM images of CoC_2O_4 precursors (**a**, **b**) and sample S1 (**c**, **d**) obtained with ultrasonic irradiation. **e** TEM and **f**–**h** HRTEM images of S1

of Co_3O_4 nanoparticles, and a large amount of pores are formed within the microrods. The distinct lattice fringes in the HRTEM image (Fig. 2f) reveal that the Co_3O_4 nanoparticles are well crystallized. Figure 2g, h shows the HRTEM images of different regions marked in Fig. 2f and the corresponding FFT images (insets). The lattice spacing of 0.41, 0.47, and 0.24 nm corresponds to the (002), (111), and (311) crystal planes of the cubic Co_3O_4 , respectively. The FFT patterns confirm each Co_3O_4 nanoparticle is single crystalline.

To study the influence of ultrasound irradiation on the products, a similar experiment was carried out without ultrasound irradiation. The SEM images of the precursors and the product S2 obtained without ultrasound irradiation are shown in Fig. 3. The precursors are aggregated bundles with large sizes (Fig. 3a, b). The Co_3O_4 bundles are formed after calcination (Fig. 3c, d); they are porous with irregular shapes, consisting of numerous nanoparticles and pores

resulted from the thermal decomposition of CoC_2O_4 precursors. The chemical effects of ultrasonic irradiation arise from acoustic cavitation, namely the formation, growth, and implosive collapse of bubbles in a liquid medium which can generate local hot spots having a temperature of roughly 5,000 °C, pressure of about 500 atm, and a lifetime of a few microseconds. In addition, ultrasonic irradiation has strong mechanical effect that can efficiently break up the aggregate and prevent nanocrystals from agglomerating [17, 18]. These special effects lead to the growth of the precursors with uniform morphology and then impact the final structure obtained by the calcination of the precursors. Contrarily, CoC_2O_4 nuclei or nanocrystals are prone to agglomerate to decrease surface energy and tension if there is no ultrasonic irradiation during the preparation, which leads to aggregated bundles with larger sizes. Therefore, the ultrasonic irradiation plays an important role in the preparation of porous Co_3O_4 microrods, which have

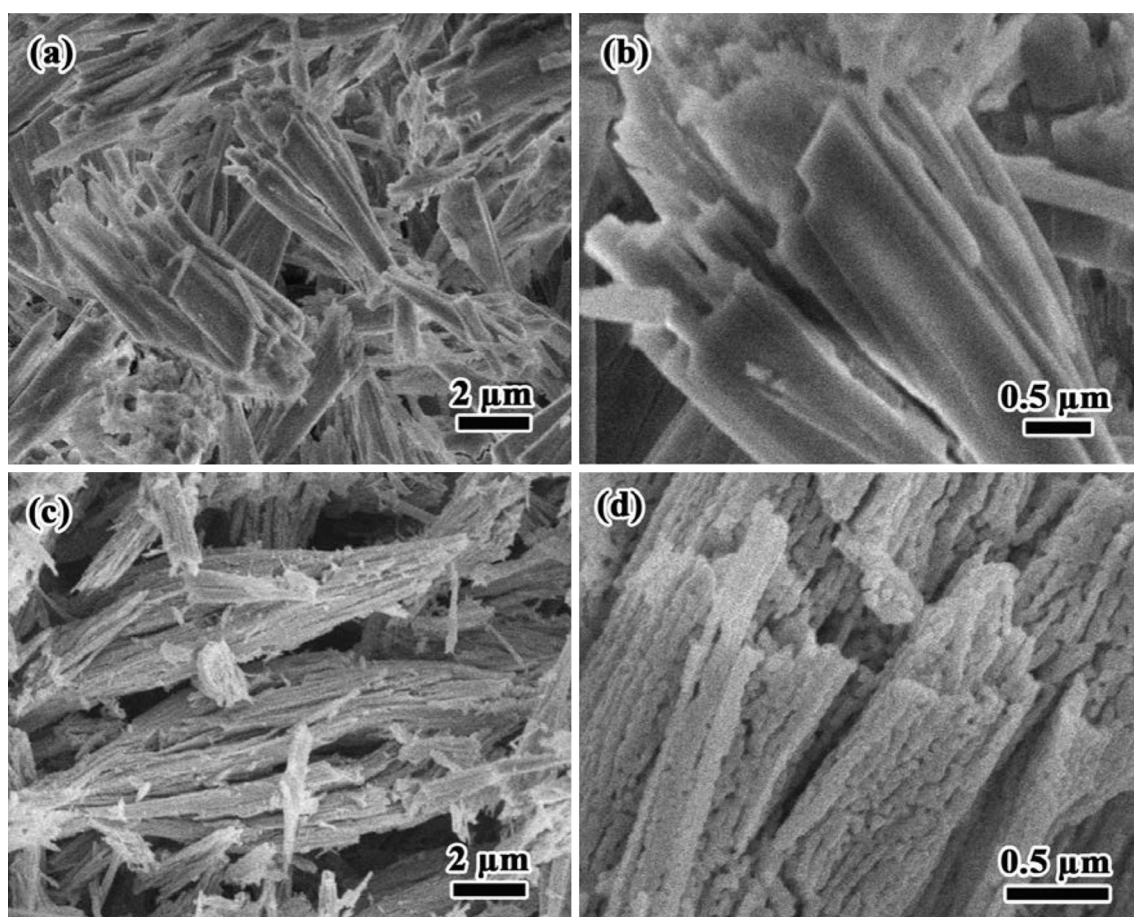
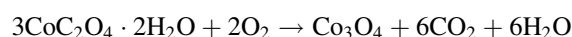


Fig. 3 SEM images of the precursors (a, b) and sample S2 (c, d) obtained without ultrasonic irradiation

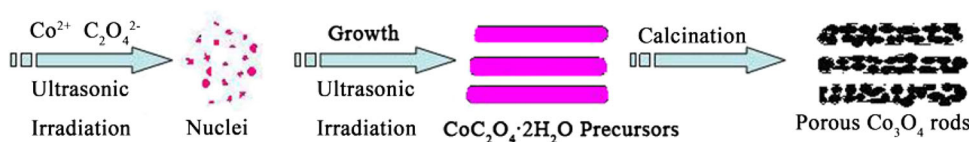
smaller size and could be advantageous for the electrochemical performance.

Porous Co_3O_4 nanorods were fabricated by adopting the ultrasonic-assisted strategy, and the formation mechanisms is illustrated in Fig. 4. First, the cobalt cations (Co^{2+}) are known to readily react with oxalic ion ($\text{C}_2\text{O}_4^{2-}$) in the dilute concentration, and then, the CoC_2O_4 nuclei are formed. The growth habit of a crystal is controlled by external environments, such as temperature, pressure, supersaturation, and solvent [18]. The CoC_2O_4 nuclei are well dispersed in the solution and grow into nanorods due to the chemical and mechanical effects of ultrasonic irradiation. Finally, upon heating, the CoC_2O_4 precursors lose water, release CO_2 , and convert to porous Co_3O_4 nanoparticles-assembled microrods by the following equation:



The lithium-storage performance of porous Co_3O_4 microrods was investigated by constant-current charge/discharge cycling. Five cells were measured for each experimental condition, and the obtained data were agreed with a deviation of about 5 mAh g^{-1} . Figure 5a shows the first, second, 10th, 20th, and 40th charge–discharge profiles at a current density of 100 mA g^{-1} . In the first cycle, the Co_3O_4 microrods (sample S1) exhibit a discharge potential plateau at $\sim 1.12 \text{ V}$ and deliver an initial discharge capacity of $1,696 (\pm 5) \text{ mAh g}^{-1}$ and a charge capacity of $1,245 (\pm 5) \text{ mAh g}^{-1}$ with a Coulombic efficiency of 73.4 %. Generally, the mechanism of Li^+ storage for oxide materials during the first discharge process includes two types. The first one is the electrolyte

Fig. 4 Schematic drawing of the formation process of porous Co_3O_4 nanorods via ultrasonic-assisted route



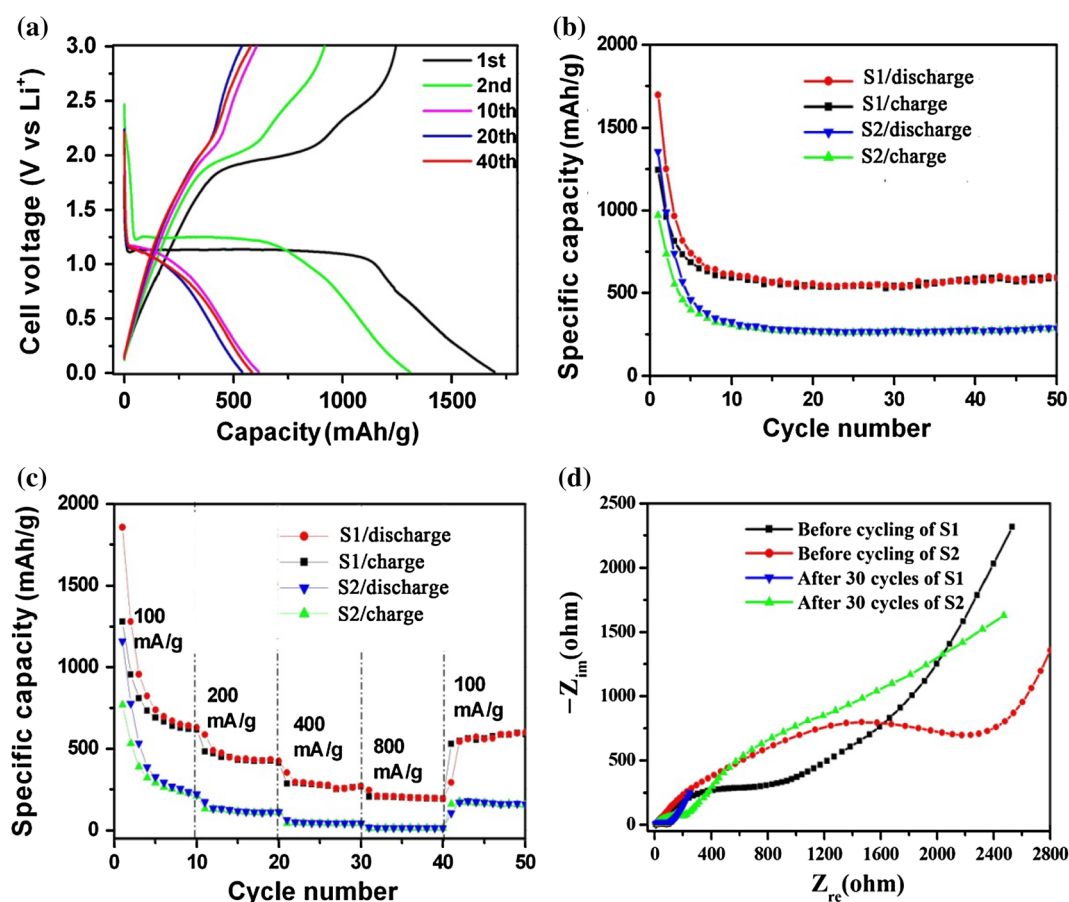


Fig. 5 **a** Voltage profiles of S1. **b** Cycling performance of S1 and S2 at a current density of 100 mA h g⁻¹. **c** Rate performance of S1 and S2. **d** Nyquist plots of S1 and S2 electrodes before cycling and after 30 cycles

decomposition and inevitable formation of a solid electrolyte interphase (SEI), which is partially irreversible. The second is a reversible redox reaction mechanism, which has been previously reported in the literature [19–21]. The conversion mechanism of Co₃O₄ in LIBs can be expressed as: $\text{Co}_3\text{O}_4 + 8\text{Li}^+ + 8\text{e}^- \leftrightarrow 4\text{Li}_2\text{O} + 3\text{Co}$. There is a plateau at ~ 2.0 V in the charge profiles. These plateaus and sloping potentials are attributed to the reversible oxidation/reduction of Co/Co₃O₄ during the Li⁺ insertion/extraction and the partially reversible formation/decomposition of SEI layer. The large capacity loss between the first and the subsequent cycles is observed, which is caused by the irreversible process, e.g., the formation of a SEI layer and drastic lithium-driven structural modifications [8]. The porous Co₃O₄ microrod electrode delivers a stable reversible capacity around 678 (± 5) mAh g⁻¹ during the 10th–50th cycles (Fig. 5b), which is much higher than the capacities of commercial anode materials (graphite 372 mAh g⁻¹) and the Co₃O₄ nanostructures recently reported in Refs [9, 12, 22, 23]. For comparison, sample S2 (Co₃O₄ bundles) shows a discharge/charge capacity of 288/286 (± 5) mAh g⁻¹ after

50 cycles. Obviously, the as-synthesized porous Co₃O₄ microrods exhibit much better capacity retention than the Co₃O₄ bundles. Furthermore, the tap density of the porous Co₃O₄ microrods is measured to be 1.32 g cm⁻³, which is much smaller than the theoretical density of Co₃O₄ (6.05 g cm⁻³). The volumetric capacity of porous Co₃O₄ was calculated by using its tap density (1.32 g cm⁻³) and its reversible capacity (678 mAh g⁻¹). The volumetric capacity is 895 mAh cm⁻³ after 50 cycles, which is still higher than the theoretically volumetric capacity of graphite electrode (830 mAh cm⁻³).

To investigate the rate capability of the Co₃O₄ products, the electrodes made of S1 and S2 were cycled at different current densities as shown in Fig. 5c. The reversible capacities of sample S1 at 100, 200, 400, and 800 mA g⁻¹ are around 622, 427, 267, and 207 mAh g⁻¹, respectively, which are much higher than those of sample S2. When the current density reduces from 800 to 100 mA g⁻¹, the discharge/charge capacity can be recovered to 600 (± 5) mAh g⁻¹ for sample S1. Apparently, the sample S1 possesses excellent high-rate capability as compared to the sample S2.

Figure 5d shows the Nyquist plots of the two electrodes before cycling and after 30 cycles in the frequency of 100 kHz to 0.01 mHz. They have the same shapes of Nyquist plots, composed of one semicircle component at high frequency and a linear component at the low frequency. Both sample S1 and S2 electrodes after 30 cycles have a smaller semicircle than that before cycling, that is to say, the charge-transfer resistance decreases after cycling. It is widely believed that the process of charge transfer occurs on active material/electrolyte interfaces, so the surface morphology of the electrode is one of the key points to affect the impedance of charge transfer [25]. The electrode volume expansion/shrinkage and the incomplete conversion reaction occurred during the first lithiation/delithiation process make Co_3O_4 nanoparticles into smaller nanograins [26], which may increase the interface/surface area of the electrode, shorten Li^+ diffusion route, and thus reduce the impedance of charge transfer due to more sufficient contact between active materials and electrolyte. Furthermore, the sample S1 shows a smaller semicircle as compared to S2 in both cases (before cycling and after 30 cycles), indicating the porous Co_3O_4 microrods (S1) have a smaller electrochemical reaction resistance than Co_3O_4 bundles (S2). In other words, the lithium ions can transfer more easily on the porous Co_3O_4 microrods/electrolyte interface. The decreasing charge-transfer resistance accounts for the enhanced electrode process kinetics and the improved electrochemical performance of Co_3O_4 microrods. In addition, as identified by SEM and TEM analysis, the porous Co_3O_4 microrods consisted of interconnected nanoparticles and inter-particle pores. During the lithiation–delithiation processes, the porous architectures of Co_3O_4 microrods have better structural flexibility for volume change, leading to the enhanced electrochemical performance as anode material for LIBs [5, 24].

4 Conclusions

Porous Co_3O_4 microrods have been prepared by a novel two-step method involving the ultrasonic-assisted synthesis of $\text{CoC}_2\text{O}_4 \cdot 2\text{H}_2\text{O}$ precursors and subsequent thermal annealing in air. The as-synthesized Co_3O_4 microrods are constructed by many interconnected nanoparticles and exhibit a unique porous architecture. The ultrasonic irradiation is found to be critical to determine the morphology and the electrochemical performance of Co_3O_4 products. As anode material for LIBs, the porous Co_3O_4 microrods exhibit improved lithium-storage capacity, better cycling stability, and rate capability, which can be attributed to the reduced electrochemical reaction resistance due to the

uniform architecture of Co_3O_4 microrods. Our results present a new approach to porous Co_3O_4 with great potential as anode material in LIBs.

Acknowledgments This work was supported by the Program for New Century Excellent Talents in University of Ministry of Education of China (NCET-11-1081).

References

1. Z.Y. Wang, L. Zhou, X.W. Lou, *Adv. Mater.* **24**, 1903 (2012)
2. S.G. Hwang, G.O. Kim, S.R. Yun, K.S. Ryu, *Electrochim. Acta* **78**, 406 (2012)
3. Q.M. Su, G.H. Du, J. Zhang, Y.J. Zhong, B.S. Xu, Y.H. Yang, S. Neupane, K. Kadel, W.Z. Li, *ACS Nano* **7**, 11379 (2013)
4. Y. Liu, H. Zheng, X.H. Liu, S. Huang, T. Zhu, J.W. Wang, A. Kushima, N.S. Hudak, X. Huang, S.L. Zhang, S.X. Mao, X.F. Qian, J. Li, J.Y. Huang, *ACS Nano* **5**, 7245 (2011)
5. D. Xie, W.W. Yuan, Z.M. Dong, Q.M. Su, J. Zhang, G.H. Du, *Electrochim. Acta* **92**, 87 (2013)
6. C. Wang, D.L. Wang, Q.M. Wang, L. Wang, *Electrochim. Acta* **55**, 6420 (2010)
7. B. Jang, M. Park, O.B. Chae, S. Park, Y. Kim, S.M. Oh, Y. Piao, T. Hyeon, *J. Am. Chem. Soc.* **134**, 15010 (2012)
8. Q.M. Su, Z.M. Dong, J. Zhang, G.H. Du, B.S. Xu, *Nanotechnology* **24**, 255705 (2013)
9. W.W. Yuan, D. Xie, Z.M. Dong, Q.M. Su, J. Zhang, G.H. Du, B.S. Xu, *Mater. Lett.* **97**, 129 (2013)
10. F. Zhang, C.Z. Yuan, X.J. Lu, L.J. Zhang, Q. Che, X.G. Zhang, *J. Power Sources* **203**, 250 (2012)
11. Y. Lu, Y. Wang, Y.Q. Zou, Z. Jiao, B. Zhao, Y.Q. He, M.H. Wu, *Electrochem. Commun.* **12**, 101 (2010)
12. J. Zheng, J. Liu, D.P. Lv, Q. Kuang, Z.Y. Jiang, Z.X. Xie, R.B. Huang, L.S. Zheng, *J. Solid Stat. Chem.* **183**, 600 (2010)
13. Y. Sun, X.Y. Feng, C.H. Chen, *J. Power Sources* **196**, 784 (2011)
14. X.H. Rui, H.T. Tan, D.H. Sim, W.L. Liu, C. Xu, H.H. Hng, R. Yazami, T.M. Lim, Q.Y. Yan, *J. Power Sources* **222**, 97 (2013)
15. P. Zhang, Z.P. Guo, Y.D. Huang, D.Z. Jia, H.K. Liu, *J. Power Sources* **196**, 6987 (2011)
16. X. Wang, W. Tian, T.Y. Zhai, C.Y. Zhi, Y. Bando, D. Golberg, *J. Mater. Chem.* **22**, 23310 (2012)
17. P. Rai, J.N. Jo, I.H. Lee, Y.T. Yu, *Solid State Sci.* **12**, 1703 (2010)
18. D. Xie, L. Chang, F.X. Wang, G.H. Du, B.S. Xu, *J. Alloys Compd.* **545**, 176 (2012)
19. H. Huang, W.J. Zhu, X.Y. Tao, Y. Xia, Z.Y. Yu, J.W. Fang, Y.P. Gan, W.K. Zhang, *ACS Appl. Mater. Interfaces* **4**, 5974 (2012)
20. Y. Liu, C.H. Mi, L.H. Su, X.G. Zhang, *Electrochim. Acta* **53**, 2507 (2008)
21. Q.M. Su, D. Xie, J. Zhang, G.H. Du, B.S. Xu, *ACS Nano* **7**, 9115 (2013)
22. S.W. Hwang, A. Umar, S.H. Kim, S.A. Al-Sayari, M. Abaker, A. Al-Hajry, A.M. Stephan, *Electrochim. Acta* **56**, 8534 (2011)
23. Y.H. Ding, P. Zhang, Z.L. Long, Y. Jiang, J.N. Huang, W.J. Yan, C. Liu, *Mater. Lett.* **62**, 3410 (2008)
24. D. Xie, Q.M. Su, Z.M. Dong, J. Zhang, G.H. Du, *CrystEngComm* **15**, 8314 (2013)
25. J.Y. Xiang, X.L. Wang, J. Zhong, D. Zhang, J.P. Tu, *J. Power Sources* **196**, 379 (2011)
26. Q.M. Su, J. Zhang, Y.S. Wu, G.H. Du, *Nano Energy* **9**, 264 (2014)